Supporting information

Superionicity by design: High Proton Conductivity in a Fluorine-free Protic Ionic Liquid

Hanno Maria Schütz[†a,b], Stefano Nejrotti[†c], Henry Adenusi[d], Alessandro Mariani[a,b,e], Enrico Bodo*[f], Matteo Bonomo*[c], Alessandro Innocenti[a,b⊥], Claudia Barolo[c], Xinpei Gao[g], Stefano Passerini*[a,b]*

[a] *Helmholtz Institute Ulm (HIU), Helmholtzstrasse 11, 89081 Ulm, Germany*

[b] *Karlsruhe Institute of Technology (KIT), P.O. Box 3640, 76021 Karlsruhe, Germany*

[c] *Department of Chemistry, NIS Interdepartmental Centre, INSTM Reference Centre, University of Turin, via Pietro Giuria 7, 10125 Turin, Italy*

[d] *Department of Science and Engineering of Matter, Environment and Urban Planning, Marche Polytechnic University, Via Brecce Bianche, 60131, Ancona, Italy*

[e] *Elettra Sincrotrone Trieste, 34012 Basovizza, Trieste, Italy*

[f] *Department of Chemistry, Sapienza University of Rome, P. le Aldo Moro 5, 00185 Rome, Italy*

[g] *School of Chemistry and Chemical Engineering, Hainan University, Haikou 570228, P. R. China*

[†] *These authors gave equal contributions*

[⊥] *Present address: Zentrum für Sonnenenergie- und Wasserstoff-Forschung Baden-Württemberg, Ulm 89081, Germany*

alessandro.mariani@elettra.eu

enrico.bodo@uniroma1.it

matteo.bonomo@unito.it

stefano.passerini@kit.edu

Contaminants

Table S1: ICP-OES measurements of [DESPA][HMDS] and the precursor [H_2MDS]. n.d.= not detectable

sample	Ca/ ppm	K / ppm	Na / ppm
[DESPA][HMDS]	157	378	583
H_2MDS	309	n.d.	1185

NMR analysis

As shown in detail in Figure S1a, in the ^{1}H NMR spectrum of [DESPA][HMDS] in DMSO-d_6 solution some additional peaks (namely, at 3.3, 2.9 and 2.6 ppm) are present. The integral of these peaks is 0.16 (when the CH_3 peak at 1.2 ppm is normalized to 6). Interestingly, the values of the integrals attributed to the CH_2 groups adjacent to NH or SO_3H in the DESPA structure, in the region 2.65–3.15 ppm, are 1.8, while the integrals of the remaining DESPA's CH_2 (at 1.9 ppm) and of the HMDS's CH_2 (at 3.8 ppm) are 2, as expected. Furthermore, an additional peak is present at 8.1 ppm, whose integral is roughly in the same ratio to the peak at 9.2 as the peaks integrating 0.16 are to those integrating 1.8. This minor "replica" of the [DESPA] spectrum suggests that a second species is present, accounting for roughly 10% of the whole population. Interestingly, the peaks attributed to the CH_2 groups of the ethyl chains are not magnetically equivalent in the "replica" spectrum, suggesting that a break of symmetry occurs in this species. This could be explained through the formation of a cyclic structure arising from an intramolecular hydrogen bond interaction between the NH and one of the oxygen atoms of the terminal SO_3H group, which would impart rigidity to the system, thus differentiating the environment experienced by the two methylene groups. This interpretation is further supported by the fact that the proton at 5.87 ppm is bound to a nitrogen atom, as evidenced by the ^{1}H-^{15}N HMQC spectrum (Figure S1b).

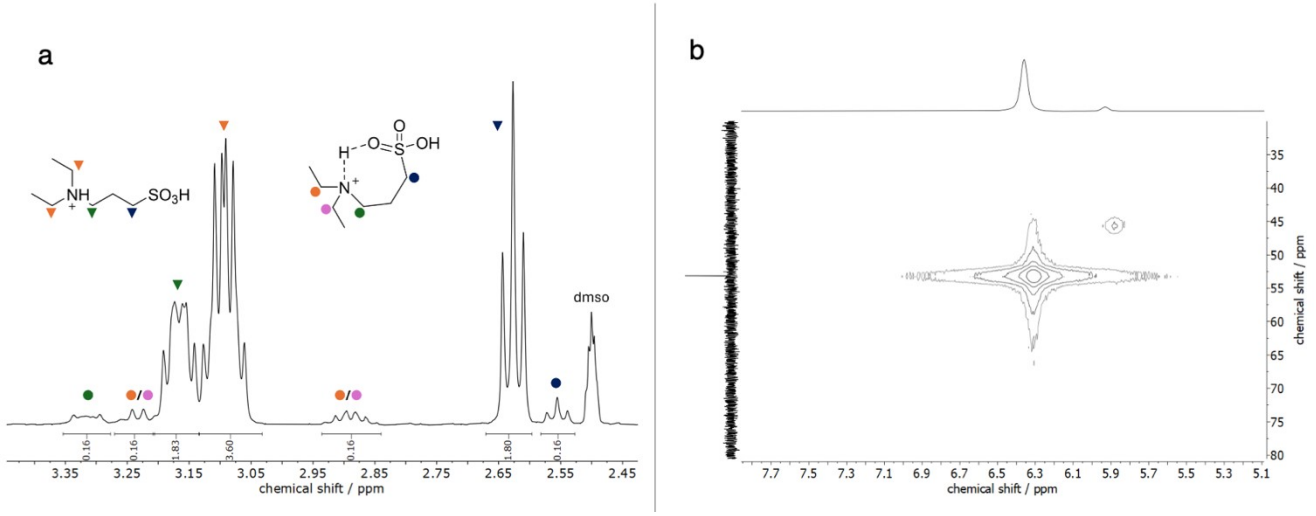

Figure S1: (a) Zoomed view of the ^{1}H-NMR spectrum of [DESPA][HMDS] in DMSO-d_6. The insets show the two possible conformers of the cation, also indicating the assignment for the duplicated peaks. (b) ^{1}H-^{15}N bidimensional HMQC NMR spectrum of pure [DESPA][HMDS].

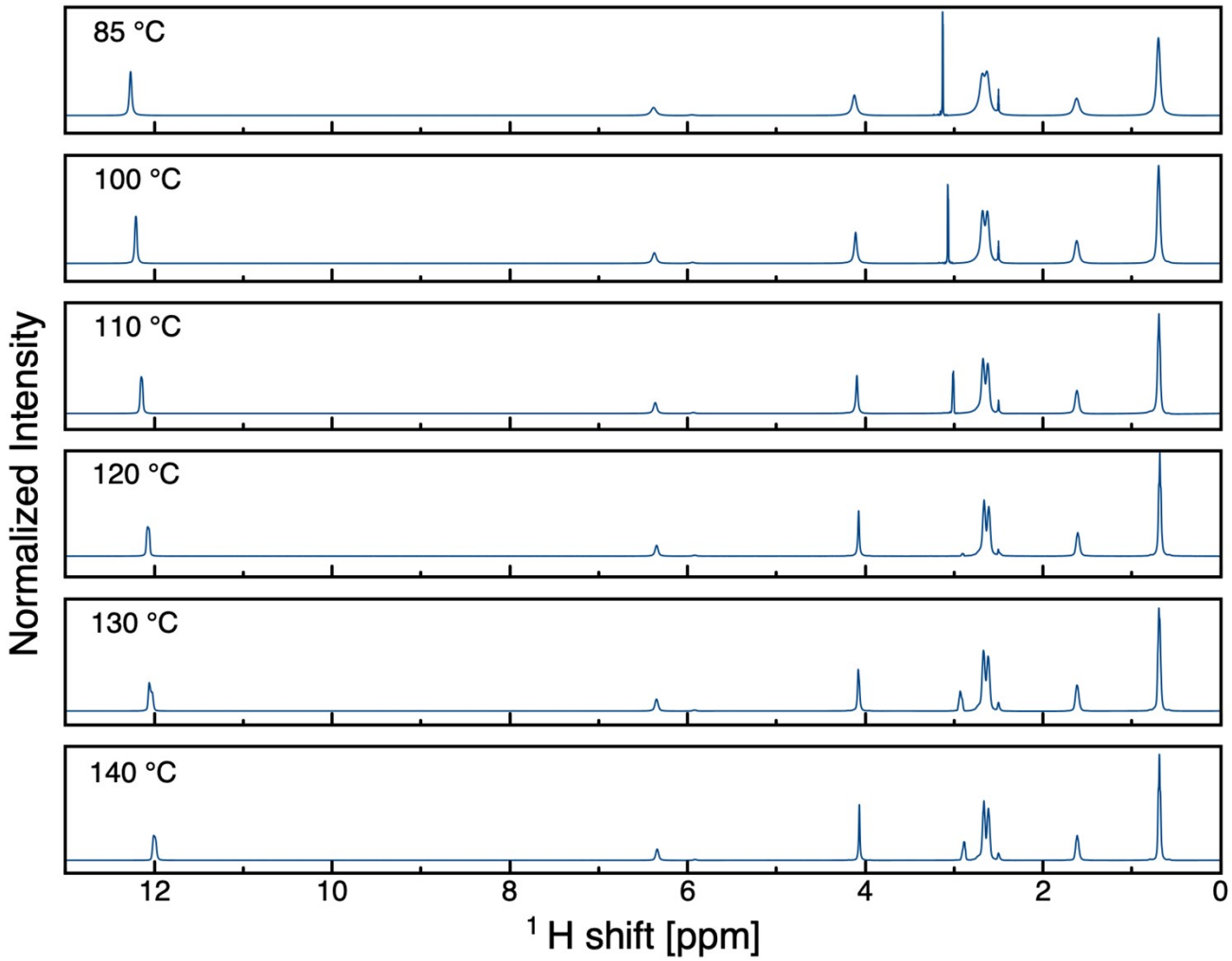

Figure S2: ^{1}H-NMR spectra of pure [DESPA][HMDS] as a function of temperature. The residual DMSO peak is from the deuterated solvent in the external tube.

Table S2: ^{1}H-NMR peaks positions, integrals, and FWHM for the pure [DESPA][HMDS] as a function of temperature. Numbers in brackets in the peak assignment correspond to the labels of the protons in Figure1 in the main text.

Temperature [K]	Proton	Position [ppm]	Integral [a.u.]	FWHM [ppm]
358	DESPA OH (7) HDMS OH (9)	12.228	2.35	0.064
		12.213		0.062
	DESPA NH (3)	6.379	0.88	0.066
	DESPA NH - Closed Ring (3')	5.959	0.06	0.059
	HDMS CH_2 (8)	4.122	2.00	0.056
	DESPA CH_2 (6)	2.679	7.97	n.d.
	DESPA CH_2 (2) DESPA CH_2 (4)	2.632		n.d.
	DESPA CH_2 (5)	1.622	1.94	0.069*
	DESPA CH_3 (1)	0.700	6.22	0.047
373	DESPA OH (7) HDMS OH (9)	12.160	2.29	0.048
		12.152		0.046
	DESPA NH (3)	6.373	0.90	0.051
	DESPA NH - Closed Ring (3')	5.940	0.07	0.05
	HDMS CH_2 (8)	4.108	2.00	0.036

	DESPA CH_2 (6)	2.678	7.96	n.d.
	DESPA CH_2 (2) DESPA CH_2 (4)	2.626		n.d.
	DESPA CH_2 (5)	1.620	2.00	0.043*
	DESPA CH_3 (1)	0.698	6.23	0.037
383	HDMS OH (9)	12.146	2.20	0.046
	DESPA OH (7)	12.136		0.044
	DESPA NH (3)	6.363	0.92	0.043
	DESPA NH - Closed Ring (3')	5.940	0.08	0.043
	HDMS CH_2 (8)	4.093	2.00	0.028
	DESPA CH_2 (6)	2.674	8.05	n.d.
	DESPA CH_2 (2) DESPA CH_2 (4)	2.620		n.d.
	DESPA CH_2 (5)	1.618	1.98	0.042*
	DESPA CH_3 (1)	0.694	6.19	0.03
393	HDMS OH (9)	12.073	2.21	0.035
	DESPA OH (7)	12.062		0.032
	DESPA NH (3)	6.355	0.90	0.039
	DESPA NH - Closed Ring (3')	5.924	0.07	0.039
	HDMS CH_2 (8)	4.081	2.00	0.027
	DESPA CH_2 (6)	2.669	7.92	n.d.
	DESPA CH_2 (2) DESPA CH_2 (4)	2.617		n.d.
	DESPA CH_2 (5)	1.615	1.98	0.038*
	DESPA CH_3 (1)	0.691	6.12	0.029
403	HDMS OH (9)	12.058	2.22	0.036
	DESPA OH (7)	12.026		0.033
	DESPA NH (3)	6.349	0.90	0.038
	DESPA NH - Closed Ring (3')	5.917	0.07	0.039
	HDMS CH_2 (8)	4.078	2.00	0.025
	DESPA CH_2 (6)	2.669	7.95	n.d.
	DESPA CH_2 (2) DESPA CH_2 (4)	2.618		n.d.
	DESPA CH_2 (5)	1.617	1.96	0.036*
	DESPA CH_3 (1)	0.695	6.08	0.028
413	HDMS OH (9)	12.007	2.23	0.036
	DESPA OH (7)	11.996		0.032
	DESPA NH (3)	6.341	0.92	0.037
	DESPA NH - Closed Ring (3')	5.901	0.07	0.038
	HDMS CH_2 (8)	4.066	2.00	0.023
	DESPA CH_2 (6)	2.663	8.07	n.d.
	DESPA CH_2 (2) DESPA CH_2 (4)	2.614		n.d.
	DESPA CH_2 (5)	1.615	2.06	0.043*
	DESPA CH_3 (1)	0.689	6.17	0.026

*Signal difficult to properly fit

The calculation of the peak width (FWHM) in 1D ^{1}H-NMR spectra could give insights on the exchange dynamics of the protons in the system. In our study, the non-resolved multiplicity of some peaks, though, make this analysis significantly challenging. In neat-state spectra, multiplets often collapse into broad signals, rendering their width incomparable to that of singlets. For instance, the peak at 0.65 ppm, which appears as a clear triplet in solution state, and the one at 1.57 ppm, a quartet in solution state, exhibit notable differences in width. This variability means that only certain peaks can be reliably used for comparison. Moreover, the high viscosity of the system at 85 °C causes data to deviate from expected trends, as evidenced by the substantial differences in width values between anion and cation peaks at this temperature. Additionally, the acidic protons around 12 ppm result from overlapping peaks, complicating their analysis. Although the width of the 12 ppm proton becomes narrower compared to NH protons at high temperatures, the necessity of fitting two Gaussians to the peak suggests a potential overparameterization issue. Therefore, the analysis of these curves is not entirely reliable for highlighting peculiar behaviors of acidic protons or heteroatom-bonded protons.

Despite these challenges, our data show that heteroatom-bonded protons consistently exhibit (ca. 1.4 times) wider peaks compared to aliphatic protons. This observation indicates their involvement in hydrogen-bond networking. Moreover, the similar widths of both closed ring and free NH peaks corroborates the hypothesis that even the free NH proton does not experiment any significant proton exchange; as such its involvement in unconventional proton hopping could be excluded. These findings suggest that the unexpectedly high conductivity observed might result from a non-vehicular charge diffusion mechanism involving the OH bonded protons, supporting a Grotthuss-(like) mechanism.

Thermal Characterization

Thermal characterization

The Differential Scanning Calorimetry (DSC) and Thermal Gravimetric Analysis of compounds relevant to this study are summarized in Table S3

Table S3: Characteristic temperatures of compounds relevant for the study. All values are expressed in Kelvin.

Compound	T_m	T_g (cooling)	T_g (heating)	T'_d (first DTG peak)	T_d (5% mass loss)
[DESPA][HMDS]	n.d.	240.15±0.4	244.35±0.1	650	584
[DEAPS]	n.d.	n.d.	n.d.	575	561
H_2MDS	364[a], 413[b]	n.d.	n.d.	562	543
K_2MDS	> 473	n.d.	n.d.	677	669

[a]Hydrated[1]; [b]anhydrous[2]

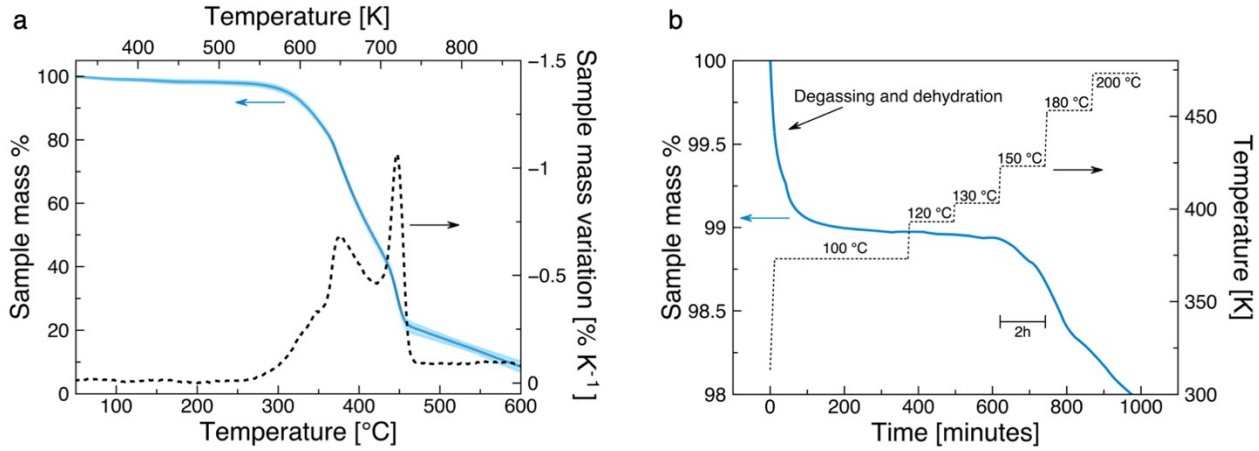

Figure S3: Thermogravimetric Analysis in synthetic air of [DESPA][HMDS]. (a) Dynamic scan at 5 °C/min (solid line) and DTGA (dashed line), the shaded area represents the uncertainty obtained with three measurements of the same batch; (b) stepwise isothermal scan. A water-content of 8362±217 ppm was determined by Karl-Fischer titration before the measurements.

The TGA experiments were performed in synthetic air, thus in much harsher conditions compared to standard TGA experiments. This choice comes from the necessity of testing the potential application of the PIL in intermediate temperature fuel cells. Regardless of the presence of oxygen, [DESPA][HMDS] displays good thermal stability with a decomposition temperature (T_d) of 650 K, well beyond the target temperature for its possible implementation in intermediate temperature fuel-cells of 393 K (Figure S3a). Such a result makes [DESPA][HMDS] stability widely superior to Phosphoric Acid (T_d 486 K)[3], better than PILs with the same cation, e.g., [DESPA] triflate and [DESPA] hydrogen sulphate (T_d 610 K and 568 K, respectively)[4], and comparable to Triethylammonium Triflate (T_d 650 K)[5], which is used in fuel cells. Traditional TGA measurements are inadequate to test the long-term stability of a compound exposed to high temperatures and oxidative atmospheres for extended periods of time. For this reason, we also performed isothermal TGA (Figure S3b), keeping the sample at 373 K for 6 h, and then increasing the temperature at 393 K, 403 K, 423 K, 453 K, and 473 K in discrete steps maintaining each temperature for 2 h. Our results show that [DESPA][HMDS] is thermally stable over an extended period above 403 K, with a mere 2% total mass loss even at 473 K. It should be noted that the initial ~1% mass loss at 373 K is most likely due to degassing and dehydration of the PIL. To ascertain the origin of the decomposition, TGA on [DESPA][HMDS] precursors and some selected relevant compounds were conducted (see Table S3 and Figure S4a). The results show that the thermal stability increases from H_2MDS to the doubly deprotonated dipotassium methanedisulfonate (K_2MDS) with T_d 562 K and 677 K, respectively. Here, it can be assumed that the thermal stability of the singly deprotonated [HMDS] anion lies between the two limiting cases. Based on the possible stabilization of [HMDS] by an intramolecular hydrogen bond and the extensive charge delocalization, the thermal stability is reasonably at the higher end of the 562-677 K. Unfortunately, this hypothesis cannot be experimentally validated because potassium hydrogen methanedisulfonate [KHMDS] is experimentally not accessible. All

attempts to prepare this salt ended in mixtures of [H_2MDS] and [K_2MDS] and not the pure monoprotonated compound. The comparison of the TGA results with the [DEAPS] zwitterion (T_d 575 K) indicate that the limiting factor for the thermal stability in [DESPA][HMDS] might be the cation decomposition.

In the DSC traces of [DESPA][HMDS], no melting/crystallization peak is visible (Figure S4b). Despite the expected strong intermolecular interactions, the PIL does not crystalize. On the other hand, at about 244 K a glass transition was observed in the heating trace (Table S3, Figure S4b). Other PILs with the [DESPA] cation display a lower glass transition temperature, *e.g.*, [DESPA] triflate and [DESPA] hydrogen sulphate show their T_gs at about 217 K and 215 K, respectively.[4,6] Neither melting point nor glass transition have been observed for the DEAPS zwitterion, which appears to decompose before melting. The melting point of K_2MDS was not observed in the temperature range tested, while for H_2MDS there are conflicting values reported in literature, which refers to different states of hydration, as highlighted in Table S3.

The density ρ of [DESPA][HMDS] decreases linearly with temperature increasing up to 353 K (Figure S4c), following the usual trend dictated by the thermal volume expansion. Taking advantage of this, density values up to 393 K (open symbols in Figure S4c) were obtained by extrapolation. This was needed to calculate the molar concentrations used for obtaining the molar conductivity values (*vide infra*). The small change in density of only 0.06 g cm^{-3} over 100 K was further analyzed by extracting the Isobaric Thermal Expansivity α (Figure S4c), which is a measure of how much the volume of a substance changes with the temperature T at constant pressure P, via

$$\alpha = -\frac{1}{\rho}\left(\frac{\partial \rho}{\partial T}\right)_P \qquad (1)$$

Compared to aprotic ILs the isobaric thermal expansivity of [DESPA][HMDS] is small, being ~4.4·10^{-4} K^{-1}. Tokuda et al.[7–9] reported values between 7.26-10.6·10^{-4} K^{-1} for ILs with different ions. Generally, for inorganic molten salts the isobaric thermal expansivity ranges between 2-5·10^{-4} K^{-1} [10]. On the other hand, similar values around 5·10^{-4} K^{-1} were found for ethylammonium nitrate[11], which is the prototypical PIL, and for other [DESPA]-based PILs.[4] The small value found for [DESPA][HMDS] is a hint for a well pronounced hydrogen-bond network, which is also the case for ethylammonium nitrate[12]. This rigid structure counteracts the thermal expansion limiting the density change with temperature.

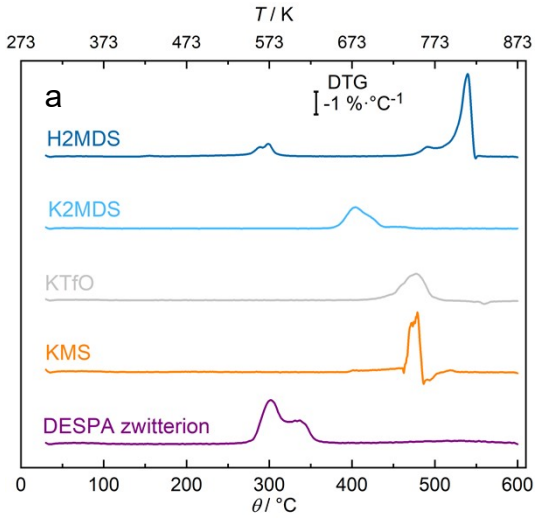

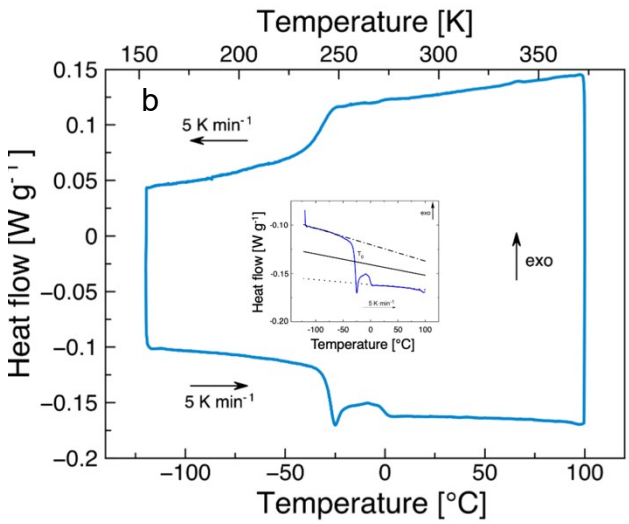

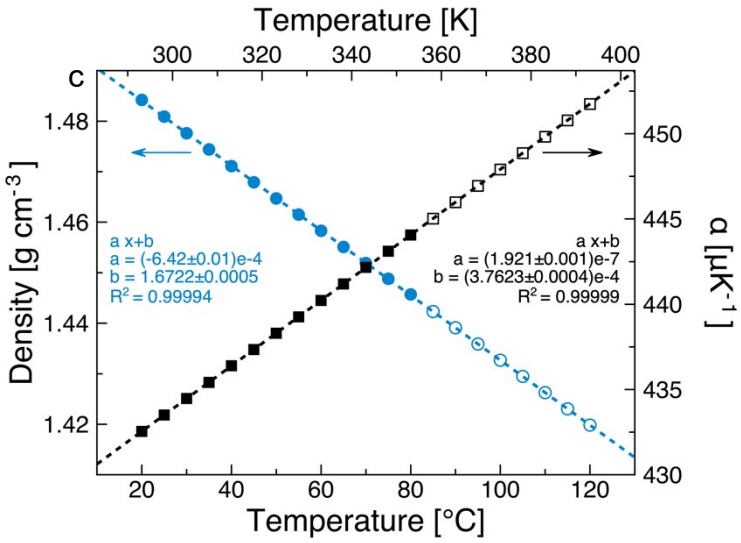

Figure S4: (a) DTGA for precursors of [DESPA][HMDS] and salts of related compounds. H_2MDS: methanedisulfonic acid, K_2MDS: dipotassium methanedisulfonate, KTfO: potassium triflate, KMS: potassium mesylate and [DEAPS] zwitterion. The experiments were performed with 5 °C·min^{-1} heating rate in synthetic air. Each curve is an average of at least three individual measurements. (b) DSC trace of [DESPA][HMDS]. The inset shows a detail of the determination of the glass transition point T_g in [DESPA][HMDS]. The doted and doted-dashed lines are the baselines for temperatures above and below T_g, respectively. The black solid line is the bisector of the two baselines. The intersection of the bisector with the DSC trace is defined as the glass transition point T_g. (c) Density (blue circles) and isobaric thermal expansivity (black squares) for [DESPA][HMDS]. The dashed lines refer to the linear fittings. Empty symbols are extrapolated on the basis of the fitting parameters.

Transport properties

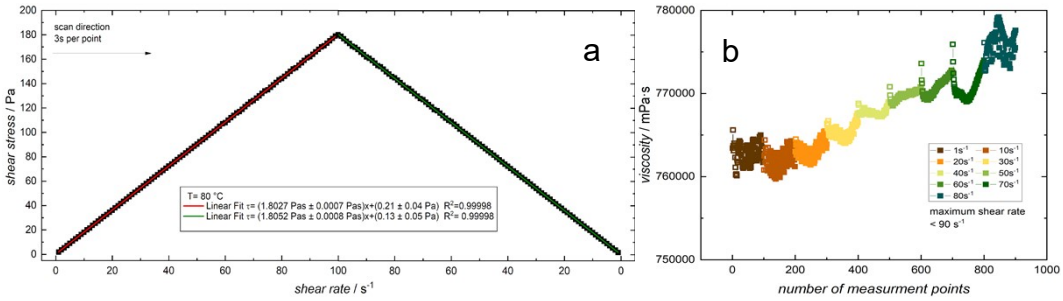

Figure S5: (a) shear-rate dependent shear-stress measurements of [DESPA][HMDS] at 80 °C. The shear rate was ramped between 1 to 100 s^{-1} in 1s^{-1} increments and each value was hold for 3 s. Experimental values (symbols) and linear regression lines are displayed (red and green lines). (b) shear rate dependent viscosity of [DESPA][HMDS] at 20 °C. The shear rate was increased from 1 to 80 s^{-1} in 10s^{-1} increments. Each step was hold for 100 point (3 s per point) to reach a constant shear flow in the high viscous liquid.

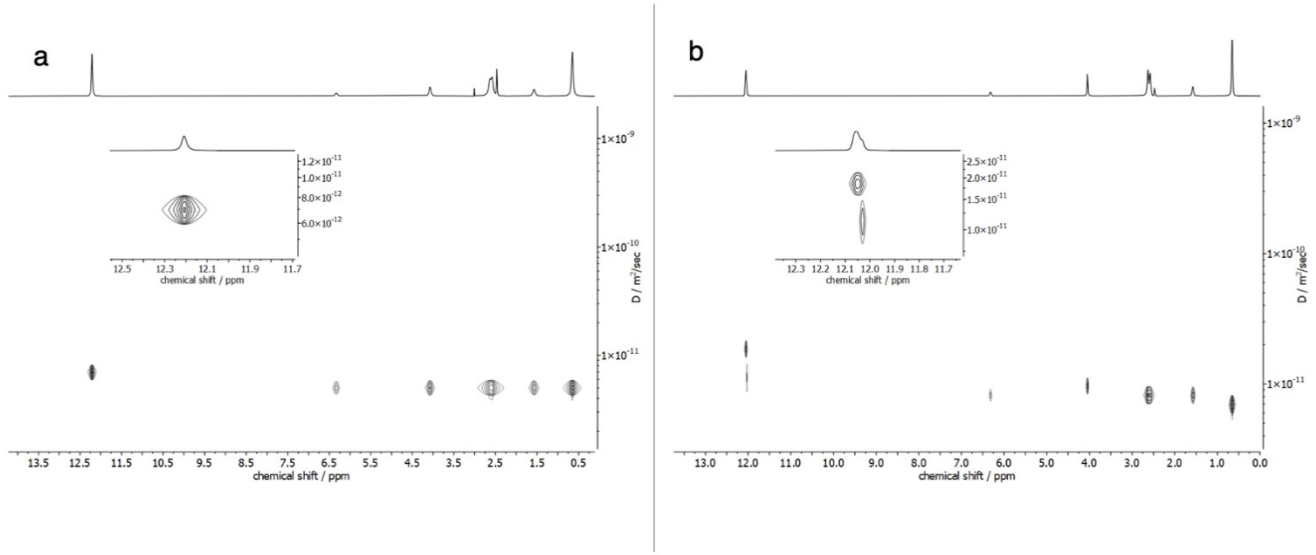

Figure S6: Bayesian representation of the DOSY PGSE ^{1}H-NMR experiments on [DESPA][HMDS]. Comparison between (a) 85 °C, and (b) 120 °C. The insets show a zoom of the OH protons signals.

Table S4: Diffusion coefficients of [DESPA] cation determined with PGSE-NMR as a function of temperature. The values are expressed in µm^2 s^{-1}. The number associated to each proton is coherent with the scheme reported in the inset of Figure 1 in the main text.

T [K]	DESPA CH_3 (1)	DESPA CH_2 (2)	DESPA CH_2 (4)	DESPA CH_2 (5)	DESPA CH_2 (6)	DESPA NH (3)
360	4.75 ± 0.32	4.85 ± 0.47	4.72 ± 0.45	5.14 ± 0.43	5.17 ± 0.48	5.17 ± 0.33
370	5.44 ± 0.40	5.69 ± 0.33	5.67 ± 0.51	5.47 ± 0.35	5.80 ± 0.69	5.76 ± 0.45
380	6.54 ± 0.54	6.65 ± 0.52	6.10 ± 0.46	6.03 ± 0.42	6.04 ± 0.82	6.26 ± 0.59
390	7.09 ± 0.74	7.65 ± 0.65	7.46 ± 0.67	7.69 ± 0.87	7.48 ± 1.00	7.73 ± 0.80
400	8.93 ± 0.86	8.77 ± 0.89	8.48 ± 0.63	8.93 ± 0.92	8.69 ± 1.23	9.07 ± 0.86
410	10.18 ± 0.82	10.06 ± 0.94	10.32 ± 0.69	10.29 ± 0.86	10.19 ± 1.04	10.52 ± 0.64

Materials and methods

Chemicals suppliers and nominal purities: For the synthesis of the cation precursor, 1,3-propane sultone was purchased from Alfa Aesar (99%), N,N-diethylamine from Sigma-Aldrich (≥99.5%). The methanedisulfonic acid was purchased from abcr (95%). Ultrapure water (>18 MΩ·cm at 25 °C) from a Milli-Q® device was used for the preparation of all aqueous solutions. All commercial chemicals were used without further treatment.

Synthesis method: The 3-(diethylammonio)propane-1-sulfonate (DEAPS) zwitterion synthesis is thoroughly discussed elsewhere[4]. We report here a summary for convenience. The process involved dissolving diethylamine and 1,3-propane sultone in acetone separately. The mixture containing the amine and acetone was then introduced dropwise to the 1,3-propane sultone and acetone combination under conditions of ice cooling and continuous stirring. This was followed by an extended stirring period on ice for an additional three hours. The mixture was then left to stir at ambient temperature over a span of three days. During this period, the zwitterion formed and precipitated. This precipitate was then isolated through filtration, cleansed with acetone, and subsequently dried at a temperature of 80 °C under vacuum.

The synthesis of [DESPA][HMDS] was carried out as follows. Initially, 10 g of DEAPS were placed in a 100 mL round-bottom flask, then dissolved in approximately 15 mL of water. Separately, a stoichiometric amount of commercial methanedisulfonic acid (H_2MDS) was mixed with 20 mL of water under ice cooling. The used H_2MDS was a hydrated form of approximate stoichiometry $H_2MDS \cdot 0.28\ H_2O$, as determined by ^{1}H-NMR (molecular weight: 181.29 g/mol). Accordingly, the total added amount of approximately 9.283 g corresponds to the equimolar quantity of the DEAPS zwitterion, *i.e.*, 51.2 mmol. The aqueous H_2MDS solution was then added dropwise to the DEAPS solution, which was also kept under ice cooling, at a rate of about one drop per second and under continuous vigorous stirring. Once the addition was completed, the ice bath was removed, and the solution was kept under stirring overnight at room temperature. Any remaining water was first removed using a rotary evaporator at 60 °C and a vacuum of 40 mbar, followed by vacuuming with an oil pump vacuum. The drying protocol involved stages at 40 °C for 12 hours, 50 °C for 3.5 hours, 60 °C for 5.5 hours, and finally 80 °C for 60 hours. After this process, a final vacuum of $1 \cdot 10^{-3}$ mbar was achieved.

Solution state NMR: ^{1}H NMR for reaction control after the PIL synthesis was performed on a Bruker Avance III, working at a 9.4 T magnetic field (^{1}H NMR operating frequency 400 MHz). Spectra of the PIL in DMSO-d_6 (VWR chemicals, 99.8%D) were recorded at 295 K with zg50 pulses. Multiplicity is reported as follows: s (singlet), d (doublet), t (triplet), q (quartet), quin (quintuplet), br (broad signal). ^{1}H NMR (400 MHz, DMSO-d_6) δ (ppm): 11.59 (br, 2H), 9.24 (br, 1H), 3.79 (s, 2H), 3.17 (td, *J* = 7.5, 5.0 Hz, 2H), 3.09 (qd, *J* = 7.3, 4.5 Hz, 4H), 2.63 (t, *J* = 6.7 Hz, 2H), 1.93 (quin, *J* = 7.0 Hz, 2H), 1.17 (t, *J* = 7.2 Hz, 6H).

Neat PIL NMR: NMR analysis was performed on a Jeol ECZR600 spectrometer, working at a 14.1 T magnetic field (^{1}H NMR operating frequency: 600 MHz). The spectra were recorded in a co-axial capillary configuration, with the PIL sample inside a flame-sealed capillary (Hilgenberg NMR tube, inner diameter: 2.36±0.03 mm); the sealing process took place in a dry room (dew point <-60 °C). To fill the highly viscous PIL in the capillaries, the samples were pre-heated to 80 °C. Then the PIL was injected into the capillaries through a cannula fitted by luer-lock connection to a syringe. The needle was inserted in the capillary through a glass Pasteur pipette. This allowed the retraction of the needle from the capillary without contamination of the capillary walls in the later flame-sealed part. During the process, all devices were heated with a heat-gun. Air bubbles were removed from the capillaries by cycles of centrifugation and heating in vacuum to 80 °C. Some DMSO-d_6 (Merck, 99.9% D) was then added as locking solvent in the space between the capillary and the NMR tube's walls, until solvent level reached the same level of the PIL into the inner capillary, thus minimizing the inhomogeneity of the magnetic field. Monodimensional ^{1}H NMR spectra were acquired at 298 K, 328 K, 358 K, 370 K, 382 K, 393 K, 403 K and 413 K, without sample spinning, and with a relaxation delay of 1 s. PGSE experiments were performed at 358 K, 373 K, 383 K, 393 K, 403 K and 413 K , applying 32 gradient amplitudes (from 0.05 to 800 mT/m), with a gradient pulse duration of 3.5 ms and a diffusion time of 0.3 s. Parameters were optimized at the higher temperature and then they were kept constant. The modification of these parameters at the lower temperature values does not improve the quality of the spectra due to the extreme viscosity of the sample. ^{15}N NMR was performed with a relaxation delay of 3 s, and by acquiring 8192 scans, in the range 0–300 ppm.

ICP-OES: The ICP-OES (Inductively Coupled Plasma Optical Emission Spectrometry) analysis was conducted using a Spectro Arcos spectrometer, provided by Spectro Analytical Instruments. For calibration purposes, the ICP multi-element standard solution IV (Merck), containing elements such as Al, B, Ba, Bi, Ca, Cd, Co, Cr, Cu, Fe, Ga, In, K, Li, Mg, Mn, Na, Ni, Pb, Sr, Tl, and Zn, was utilized. In a typical procedure, 50-70 mg of the PIL sample were dissolved

in aqua regia. The sequence of measurements included a calibration step using the standard, a blank test with ultra-pure water (MilliQ®), and the actual sample analysis. To ensure accuracy, these blank tests were intermittently conducted in between the analyses of the samples.

Water quantification: The water-content of [DESPA][HMDS] was determined by Karl-Fischer titration using the C30 coulometric Karl-Fischer titrator (Mettler Toledo). The device was checked before each measurement series with a water standard (Karl-Fischer water calibration standard, 100 ppm in anisole, VWR chemicals). The PIL was directly injected in the Karl-Fischer reagent (Aquastar® CombiCoulomat fritless Karl Fischer reagent, Merck). To assure complete dissolution of the PIL, the reagent solution was stirred for 300 s between the injection and the titration's start. The device was installed inside a dry room (dew point <-60 °C) to minimize the drift and allow direct sample injection in the titrator without a septum.

Thermogravimetric measurements: TGA was performed with a TG 209 F1 Libra (Netzsch) under a flow of synthetic air obtained by 8 $mL \cdot min^{-1}$ O_2 (AIR LIQUIDE, 99.9999%) and 32 $mL \cdot min^{-1}$ N_2 (house supply). After 30 min equilibration at 30 °C the samples were heated at 5 $°C \cdot min^{-1}$ up to a maximum temperature of 600 °C. The thermobalance was protected during the experiments by a 20 $mL \cdot min^{-1}$ N_2 flow. Each sample was prepared directly before the TGA measurement to exclude alterations during storage. About 2-3 mg of specimen were sealed in hermetic aluminum crucibles (DSC-crucibles, 25 µL Netzsch) inside a dry-room (dew point: <-60 °C) to prevent water uptake from the environment. After the insertion of the crucible in the TGA furnace, the lid was pierced by the autosampler (Netzsch). The experiments where repeated three times and the values were averaged. An automatic baseline correction, considering the thermal buoyancies, heat rate, gas flow etc., was performed with the TG-BeFlat® algorithm (Netzsch). To precisely control the sample temperature the sample temperature calibration (STC) function of the device was used allowing the heat release or consumption by chemical reactions in the sample to be monitored with a thermal sensor in the sample holder and the heating rate to be adjusted accordingly. This sensor was used for the temperature calibration of the oven with melting point standards (Netzsch Calibration Kit), as well. The measurements and calibrations were performed with the Netzsch measurement software (Version 6.1.0, 11.07.2014). Isothermal TGA was performed with a Discovery TGA (TA Instruments). The sample was sealed in a hermetic aluminum crucible (Discovery TGA & Q5000 IR, 80 µL) inside a dry-room (dew point: <-60 °C) to avoid any water-uptake. The lid of the crucible was perforated by the autosampler prior to the measurement. An empty crucible (nominally identical to the sample one) was used as counterweight on the balance scale. A synthetic air atmosphere with the same composition as per the dynamic TGA measurements was set with the Trios software (v3.2.0.3887). We identified the decomposition temperature using two different approaches: (i) 5% mass-loss threshold; (ii) the first maximum in the DTGA curve. The first method is the most widely used, but it is more affected by dehydration processes, which could be dramatic in PILs. The second approach is virtually unaffected by water loss, but it describes the fastest rate of mass loss rather than the onset temperature of decomposition.

Differential Scanning Calorimetry measurements: DSC experiments were performed with a Discovery DSC (TA Instruments). The samples were sealed into hermetic aluminum crucibles (Tzero® crucibles) inside a dry-room (dew point: <-60 °C). Therefore, the headspace in the crucibles were filled with dry air, and the results refer to the thermal behavior of the samples in dry air. To avoid contaminations, i.e., by atmospheric moisture, the measurement cell was always kept at 40 °C between the experiments and was flushed with N_2 (house supply), when performing a DSC run. The standard measurement procedure consisted of an initial equilibration step at 40 °C for 30 min, followed by a cooling-heating cycle with 5 $K \cdot min^{-1}$. DIN 51007 and ASTM E 1356 describe different approaches for the determination of the glass transition temperature, T_g, by the "mid-point method". However, both methods rely on tangents and are therefore in some cases, especially with a large enthalpy relaxation peak, less reliable. The evaluation of the T_g was performed with an inhouse developed variation of the mid-point method. A linear baseline was fitted before and after the step by the glass transition. The intersection of the bisector of these two baselines with the DSC trace is defined as T_g.

Density measurements: The density was recorded with an DMA 4100 M density meter (Anton Paar). Due to the high viscosity of [DESPA][HMDS], trapped air bubbles were removed under vacuum at 80 °C (~17 h). The sample was then directly injected into the pre-heated device (80 °C). The density values were acquired in 5 °C steps between 80 °C and 20 °C. Each step was performed until the instrumental stability criteria was reached. The maximum difference between a cooling and a consecutive heating cycle was 0.0001 $g \cdot cm^{-3}$, confirming the bubble-free injection and high reproducibility of the measurements.

Conductivity measurements: For the conductivity measurement the PILs were sealed inside the dry-room (dew point: <-60 °C) in High Temperature Conductivity Cells (HTCC) from Materials Mates. The cells consist of two parallel platinized platinum electrodes on a borosilicated glass holder. The cell constant was determined before each experiment with a 0.01 M KCl standard solution (1.41±0.02 mS cm^{-1} at 25 °C, VWR chemicals). The conductivity was obtained from electrical impedance recorded for 27 frequencies in the range from 50 kHz to 100 Hz with a MCM 10 Multichannel Conductivity Meter (Materials Mates & BioLogic). The modulus of the impedance at the frequency with the smallest modulus of the phase angle was automatically converted with the cell constant into the specific conductivity of the sample by the MultyC software (Material Mates) of the instrument. This set-up of HTCC and MCM10 allows measurements between 2 µS·cm^{-1} to 200 mS·cm^{-1}. An inaccuracy of less than 4% is achieved within the whole conductivity range according to the technical documentation of the instrument. The temperature of the samples is controlled with a WTSH 10 Peltier based temperature control unit (Materials Mates). The WTSH 10 unit operates between -40 °C to +150 °C and has a nominal accuracy according to the technical datasheet of ±0.1 °C. In a typical measurement the sample is heated from 25 °C to 120 °C in 5 °C or 10 °C steps. Each temperature step took 1 hour and conductivity values within ±0.1 °C of the target temperature were accepted and averaged for the reported specific conductivity values.

Viscosity measurements: Rheology measurements were performed utilizing an MCR 102 Rheometer from Anton Paar. To minimize water uptake, which could affect the measurements, the samples were handled exclusively in the dry-room (dew point:<-60 °C). The viscosity measurements were conducted using a plate-plate geometry with a diameter of 25 mm and a 100 µm gap, made of titanium to withstand the potentially corrosive nature of the PIL. This setup provided precise temperature control via a Peltier-heated P-PTD200/DI base plate and an H-PTD200 actively heated geometry housing. We first verified the Newtonian behavior of the fluids performing measurements at 80 °C across a shear rate range of 1-100 s^{-1}, and 20 °C up to 80 s^{-1}. Only a minimal change in viscosity was observed confirming the viscosity is independent from the applied shear rate (see Figure S5). Based on these findings, a constant shear rate of 10 s^{-1} was selected for the temperature-dependent viscosity measurements. The sample was introduced into the pre-heated rheometer and the temperature have been gradually adjusted in 5 °C steps. At each temperature step, the viscosity was assessed by recording 100 data points at the constant shear rate, while each point was averaged over three seconds. The variation between the initial and final viscosity in a cooling-heating cycle remained within a 10% range.

Vogel-Tammann-Fulcher and Walden analysis: We used a custom Python code (IonFit) for the Vogel-Tammann-Fulcher (VTF) and Walden analysis. The code is designed to analyze and visualize temperature-dependent properties of materials, specifically viscosity, conductivity, and density. It leverages the VTF equation to model temperature-dependent properties, as well as the Walden equation to correlate ionic mobility and viscosity. IonFit requires different input data depending on the desired result. It can work on single datasets of viscosity or conductivity, and, in that case, it will provide only the VTF fitting results for that specific quantity. If both viscosity and conductivity data are provided, it will perform the VTF analysis on each single dataset, and then it will re-iterate the two fitting simultaneously with the constrain that the obtained T_0 values must be the same for both fittings. Finally, if the user also provides the density dataset and the system's composition information, IonFit will also perform the Walden analysis returning the Walden plot and the calculated Walden Ionicity, which is a measure of the degree of dissociation of the ions in the system. The input dataset must be provided as plain text files (the extension of the file is not important, commonly used extensions such as .dat, .txt, .csv are all accepted) organized in two tab-separated columns. The first column must indicate the temperature in Kelvin, while the second contains the actual value of the measured property. The files may or may not have a single header line containing the descriptors of the columns, in case the header is present, it will be ignored by the program. The viscosity data may be provided in units of mPa s, Pa s, cP, or P, while the conductivity data may be expressed in mS cm^{-1}, or S cm^{-1}. Finally, the density data are accepted in either g cm^{-3} or kg m^{-3}. IonFit's input is a single config.ini file which contains all the needed information to calculate the desired quantities. The user is guided in the filling of the file via extensive comments and examples. More details on the code, its functionalities, and several examples are provided below. The code is available at the repository indicated in the Associated Content section in the main text.

Computational method: ab-initio calculations on isolated ions and ionic pairs were done using the Orca package.[13] The most stable geometry of the isolated ions and the homodimeric and heterodimeric ionic couples (anion-anion, anion-cation and cation-cation) was computed using the r^2SCAN-3c composite method[14] after a preliminary conformer selection performed with the tool "crest"[15] employing the GFN2-xTB method.[16] All

calculations were performed using an implicit solvent model through the C-PCM/SMD method[17,18] with the parameters of acetonitrile. The implicit solvent is needed to stabilize the like-charge complexes that are otherwise unstable in gas phase. To locate the transition state for proton transfer, the Nudged Elastic Band (NEB) method was used.[19] A first set of NEB computations was performed with r^2SCAN-3c. The same NEB search was then repeated using ωB97X-D3[20] with the def2-TZVP basis set to strengthen the reliability of the first round of findings. A small cluster consisting of four molecular species was used as a model system to explore the proton exchange events that follow and initial proton transfer from the SO_3H of a cation to the SO_3^- of the anion. The initial configuration of the cluster was composed by a cation, an anion, a deprotonated cation (a zwitterionic molecule) and a protonated anion (a neutral molecule). The proton that has been transferred onto the anion yielding the neutral specie was held in place by a suitable constraint. Starting from the zwitterion/neutral/cation/anion structure, 4 MD trajectories have been computed using the GFN2-xTB method within the xTB software.[21] Each trajectory was generated using an implicit acetonitrile solvent and at a temperature of 383 K through a Berendsen thermostat. Apart from the specific O-H bond in the initially neutral specie, the system was left to evolve without any additional constraint. Each trajectory lasted for 100 ps with a timestep of 0.5 fs.

IonFit software:

IonFit's architecture is built upon a foundation of modular functions, each tailored to a specific aspect of electrolyte analysis. The *joint_fit* function performs a joint fitting procedure on both viscosity and conductivity data arrays using the VTF equation. This fitting ensures that the T_0 parameter in the VTF equation is maintained consistently for both properties, a novel approach that has showcased commendable results in our testing. The simultaneous fitting uses as initial guess the fitting parameters obtained by the stand-alone fittings, but it uses a single value for T_0 which is initially set to be the average between the two values obtained. The *joint_fit* function then proceeds fitting the five parameters, i.e. η_0, σ_0, $E'_{a\eta}$, $E'_{a\sigma}$, and T_0, with the latter being bounded to be in the range defined by the originally obtained $T_{0\eta}$ and $T_{0\sigma}$ (the subscripts $_\eta$ and $_\sigma$ refer to the quantities obtained in the viscosity and conductivity fits, respectively). The final result is obtained by minimizing the sum of the RMSs of the two fittings. It is important to note that usually viscosity values are much larger than the conductivity ones, thus IonFit uses a weight factor to mitigate this problem. Such a factor is defined in a way that gives the same weight to the two properties if it is set equal to 0.5, and the lower the value, the lower is the weight of viscosity. Typical values found to be well-performing during our test spans between 0.0002 and 0.2, according to the specific electrolyte subject of the analysis.

Complementing this is the *walden_analysis* function, which employs the density data array to compute the molar conductivity and fluidity, needed to produce the Walden plot, and also returns the Walden ionicity. An essential step in the Walden analysis is the computation of the effective molality of the ionic species. In systems containing only ionic species, this calculation is straightforward. The equation is

$$[ions] = \frac{\rho}{1000 \cdot MW_{eff}} \qquad \text{(S1)}$$

where *[ions]* is the molarity (mol l^{-1}) of the ionic species, ρ is the mass density (g cm^{-3}) of the system, and MW_{eff} is the effective molecular weight of the ionic species. By effective molecular weight we mean the molecular weight of the hypothetical molecule representing the minimal formula of the system. As an example, the effective molecular weight of the system $(Pyr_{31}FSI)_{12}(Pyr_{31}TFSI)_7(LiTFSI)$ is 342.32 g mol^{-1}.

The presence of non-ionic species complicates the calculation of this quantity. The effective molality represents the concentration of ionic species in the solution, adjusted for the presence of non-ionic species. Typically, the molality is computed by dividing the amount of solute (in moles) by the mass of the solvent (in kilograms). In the case of systems with non-ionic species, we consider the non-ionic part to be the solvent, and it is crucial to subtract the contribution of these species to get an accurate measure of the ionic concentration. IonFit's approach is that for each species in the system, the program fetches the mole abundance *N*, molecular weight, and ionic nature. Depending on whether the species is ionic or not, its contribution to the total ionic moles and the weighted sum of molecular weights is updated. The effective molecular weight for the ionic species is computed using the formula:

$$MW_{eff} = \frac{\sum_i MW_i \cdot N_i}{n_{ionic}} \qquad \text{(S2)}$$

Where *i* indicates the ionic species, and n_{ionic} is the total amount of moles of ions. The moles in 1 kg of solvent (i.e. 1 kg of non-ionic species) is then computed and used to calculate the moles of ionic species via the knowledge of the mole fractions of every component. In this way we obtain the molality of the ionic species, which is finally converted in the molarity with the use of density data, as in Equation S1.

The program also offers the possibility to use a temperature-dependent factor to multiply the σ_0 parameter in the VTF equation. Such a factor is equal to $T^{-1/2}$ and is commonly used when performing the VTF analysis. Due to its wide popularity and an origin supported by scientific evidence [22], we decided to include it as an option during the analysis. Once the analysis is complete, the program visualizes the data using various plots, which should be exploited to check the goodness of the process and eventually lead to the tweaking of some parameters by the user in order to obtain better results. The output data is saved in text files and .png images within a timestamped directory. The main output file containing the fitted parameters is called "fitting_parameters.txt".

At the forefront of our analysis is the Vogel-Tammann-Fulcher equation (Equation 1 in the main text), the already described fundamental relationship that describes the temperature dependence of dynamic properties such as viscosity and conductivity. Through IonFit, we performed a comprehensive analysis to derive VTF fitting parameters for a vast selection of literature data sets.

Table S5 contains the results obtained for the viscosity values fitted with IonFit. The selected datasets provided the coverage of a range of viscosities from 1.88 mPa s to 613 mPa s, thus including more than two orders of magnitude. The vast majority of the state-of-art electrolytes used for the battery industry and related research falls in this wide viscosity range. The quality of the fitting is testified by the R^2 and RMS values, and by visually inspecting Figure S7. For all tables, the reader is encouraged to find the definitions of the abbreviations used in the corresponding section at the end of this document.

In Table S6 the focus is on conductivity, which is arguably the most relevant property when discussing about electrolytes. For this reason we made sure to cover the widest range possible with our tests, with particular attention to the region around 1 mS cm^{-1}. The selected datasets covered overall a range between 0.13 mS cm^{-1} and 40 mS cm^{-1}. Again, the quality of the fitting is clearly demonstrated by the R^2 and RMS quantifiers and by the results illustrated in Figure S8. For the Conductivity of $N_{4HHH}NO_3$ (green in Figure S8a, indicated with a star in Table S6) the value of σ_0 and the graph trend do not appear in line with the rest of the tested samples. Butylammonium Nitrate is known to be a super-cooled liquid at room temperature, and thus behaving peculiarly. We decided to maintain the result here in order to attract the attention on the fact that the user should always check the results obtained with IonFit and not blindly trust it. While robust and reliable, the output of the code is inherently dependent on the input data. In this specific case, the shear amount of data points was not enough to grasp the characteristics of the system, especially because the dataset comprises temperatures at and around the supercooled regime of $N_{4HHH}NO_3$.

Table S5: VTF fitting parameters obtained with IonFit for viscosity data.

System	η_0 [mPa s]	E'_a [kJ mol^{-1}]	T_0 [K]	RMS	R^2
Protic Ionic Liquids					
$N_{2HHH}NO_3$[23]	0.223	-6.329	148.782	0.04941	1.0000
$N_{3HHH}NO_3$[23]	0.194	-7.136	154.094	0.06929	1.0000
$N_{4HHH}NO_3$[23]	0.118	-8.839	141.385	0.18510	0.9996
N_{222H}TFA[24]	0.167	-5.938	159.710	0.03415	1.0000
N_{222H}MS[24]	1.179	-3.022	220.106	0.26750	0.9999
N_{222H}TfO[24]	0.165	-8.078	129.778	0.03003	1.0000
Aprotic Ionic Liquids					
Im_{11}TFSI[9]	0.290	-4.881	178.120	0.06800	0.9999
Im_{41}TFSI[9]	0.253	-5.197	180.380	0.12889	0.9996
Im_{41}BETI[7]	0.170	-6.344	180.670	0.28439	0.9995
Im_{41}TFA[7]	0.111	-6.552	177.390	0.08573	0.9997
Im_{41}TfO[7]	0.376	-4.793	193.660	0.87451	0.9993
Im_{81}TFSI[8]	0.159	-6.668	173.650	0.12742	0.9997
Pyr_{41}TFSI[9]	0.298	-5.412	181.550	0.16339	1.0000
Pyr_{31}FSI – Pyr_{31}TFSI 3:2[25]	0.252	-6.413	148.103	0.12190	0.9999
Salt in Ionic Liquids					
Pyr_{41}FSI – LiFSI 4:3[26]	0.194	-7.633	168.140	0.06793	1.0000
Pyr_{31}FSI – Pyr_{31} TFSI – LiTFSI 12:7:1[25]	0.320	-5.909	159.200	0.06994	1.0000
Pyr_{31}FSI – Pyr_{31} TFSI – LiTFSI 6:3:1[25]	0.278	-6.302	159.122	0.10600	1.0000
Pyr_{31}FSI – Pyr_{31} TFSI – LiTFSI 3:1:1[25]	0.168	-8.044	147.014	0.36990	0.9999
Locally Concentrated Ionic Liquids					
Pyr_{41}FSI – LiFSI – BTFE 4:3:4[26]	2.117	-2.689	202.706	0.66630	0.9995

$Pyr_{41}FSI$ – LiFSI – BTFE 2:1:2[27]	0.573	-4.517	179.160	0.16560	1.0000
$Im_{21}FSI$ – LiFSI – BTFE 2:1:2[27]	2.616	-1.525	226.997	0.44400	0.9994
$Im_{21}FSI$ – LiFSI – MFB 2:1:2[28]	7.704	-0.34	255.031	0.62300	0.9913
$Im_{21}FSI$ – LiFSI – DFB 2:1:2[29]	3.344	-1.06	229.818	0.34620	0.9981
Water-in-salt Electrolytes					
LiPTFSI : LiTfO 15m : 5m[30]	0.211	-6.768	163.232	0.37810	0.9999
LiPTFSI : LiTfO 19m : 5m[30]	0.132	-8.732	152.573	0.74590	1.0000
LiPTFSI 20m[30]	0.116	-8.281	154.674	0.36170	1.0000
Salt in Organic Solvent					
$LiPF_6$ 1M in EC:DMC 50:50[31]	0.159	-3.781	159.274	0.02152	0.9994

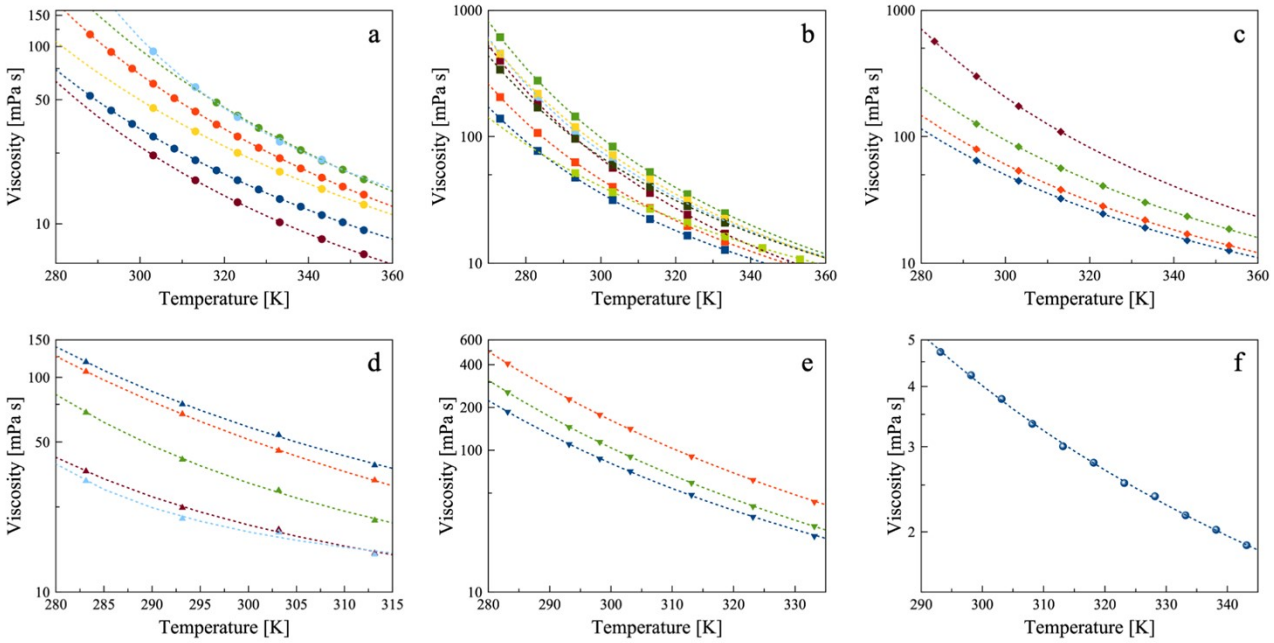

Figure S7: Results of the viscosity VTF fitting on the systems in Table S5. (a) Protic Ionic Liquids, (b) Aprotic Ionic Liquids, (c) Salt in Ionic Liquid, (d) Locally Concentrated Ionic Liquid Electrolytes, (e) Water-in-Salt Electrolytes, (f) Salt in Organic Solvent. For each panel, the color order is blue, red, green, brown, cyan, yellow, gray, light green. The order corresponds to the order in Table S5

.

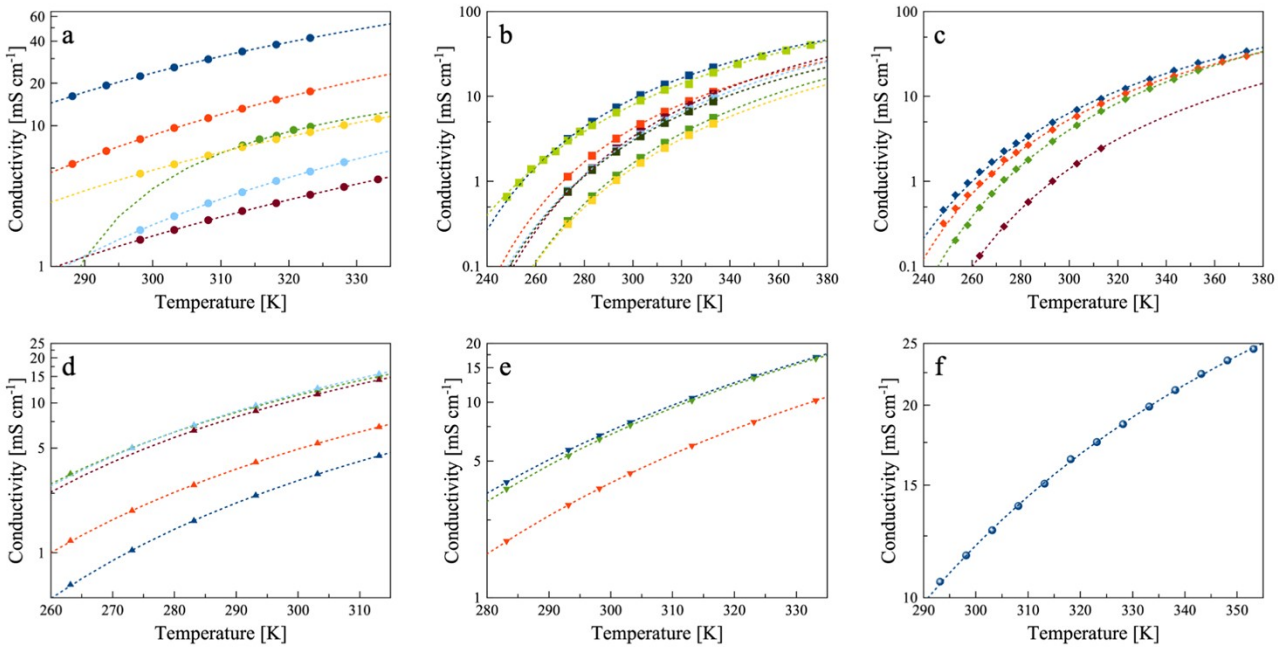

Figure S8: Results of the conductivity VTF fitting on the systems in Table S6. (a) Protic Ionic Liquids, (b) Aprotic Ionic Liquids, (c) Salt in Ionic Liquid, (d) Locally Concentrated Ionic Liquid Electrolytes, (e) Water-in-Salt Electrolytes, (f) Salt in Organic Solvent. For each panel, the color order is blue, red, green, brown, cyan, yellow, gray, light green. The order corresponds to the order in Table S6.

Table S6: VTF fitting parameters obtained with IonFit for conductivity data

System	σ_0 [mS cm^{-1}]	E'_a [kJ mol^{-1}]	T_0 [K]	RMS	R^2
Protic Ionic Liquids					
$N_{2HHH}NO_3$[23]	1062.273	4.113	169.825	0.03141	1.0000
$N_{3HHH}NO_3$[23]	1019.834	5.240	168.116	0.01820	1.0000
$N_{4HHH}NO_3$[23] *	37.932	0.605	269.19	0.06718	0.9947
$N_{222H}TFA$[24]	1070.276	10.728	100.813	0.00814	0.9999
$N_{222H}MS$[24]	266.338	4.355	193.197	0.01051	0.9999
$N_{222H}TfO$[24]	426.411	5.343	156.604	0.00792	1.0000
Aprotic Ionic Liquids					
$Im_{11}TFSI$[9]	660.893	4.673	168.200	0.04479	0.9989
$Im_{41}TFSI$[9]	430.121	4.698	178.380	0.01550	0.9994
$Im_{41}BETI$[7]	710.545	6.618	169.500	0.63566	0.9996
$Im_{41}TFA$[7]	920.737	5.978	172.320	0.00620	0.9993
$Im_{41}TfO$[7]	980.454	6.593	162.820	0.00996	0.9995
$Im_{81}TFSI$[8]	610.161	6.743	166.860	0.01125	0.9998
$Pyr_{41}TFSI$[9]	560.973	5.612	171.960	0.03751	0.9995
$Pyr_{31}FSI$ – $Pyr_{31}TFSI$ 3:2[25]	1795.258	7.630	130.777	0.41530	0.9989
Salt in Ionic Liquids					
$Pyr_{41}FSI$ – LiFSI 4:3[26]	683.898	6.872	166.519	0.00129	1.0000
$Pyr_{31}FSI$ – Pyr_{31} TFSI – LiTFSI 12:7:1[25]	1107.710	6.507	148.412	0.20780	0.9996
$Pyr_{31}FSI$ – Pyr_{31} TFSI – LiTFSI 6:3:1[25]	824.398	5.887	159.605	0.11410	0.9998
$Pyr_{31}FSI$ – Pyr_{31} TFSI – LiTFSI 3:1:1[25]	1409.268	6.832	159.842	0.05352	0.9999
Locally Concentrated Ionic Liquids					

$Pyr_{41}FSI$ – LiFSI – BTFE 4:3:4[26]	215.618	4.751	165.985	0.00821	1.0000
$Pyr_{41}FSI$ – LiFSI – BTFE 2:1:2[27]	262.746	4.636	159.880	0.01311	1.0000
$Im_{21}FSI$ – LiFSI – BTFE 2:1:2[27]	331.299	3.925	160.458	0.02220	1.0000
$Im_{21}FSI$ – LiFSI – MFB 2:1:2[28]	383.546	4.051	160.953	0.02059	1.0000
$Im_{21}FSI$ – LiFSI – DFB 2:1:2[29]	292.546	3.674	166.888	0.00089	1.0000
Water-in-salt Electrolytes					
LiPTFSI : LiTfO 15m : 5m[30]	844.800	5.930	150.520	0.01778	1.0000
LiPTFSI : LiTfO 19m : 5m[30]	654.488	6.081	157.433	0.01090	1.0000
LiPTFSI 20m[30]	608.451	4.984	166.417	0.03277	0.9999
Salt in Organic Solvent					
$LiPF_6$ 1M in EC:DMC 50:50[31]	131.709	2.487	174.795	0.07021	0.9997

Vogel-Tammann-Fulcher Restricted Fittings:

Viscosity is a property intertwined with conductivity, and S4 showcases the constrained VTF fitting parameters which is based on this strong link between these two transport properties. The constraint, ensuring a consistent T_0 parameter across both properties has a solid theoretical background. Based on the actual definition of T_0, it appears clear how it must remain consistent across derivations. From the original theory[32–34], T_0 is referred as the temperature at which the free volume available for the molecules to move is zero[22]. If that is the case, the free volume would be zero always at the same temperature for a given system regardless of which property has been used to obtain such information. This approach has been pivotal in achieving results that are both scientifically sound and consistently reliable. Table S8, which reports the results of the constrained VTF on the conductivity side, strengthen these conclusions. While it is possible to observe a general slightly worst quality of the fittings, testified by larger RMS and smaller R^2 values as shown in Tables S7 and S8, the overall reliability of the fittings is still more than satisfactory.

Table S7: VTF constrained fitting parameters obtained with IonFit for viscosity data.

System	η_0 [mPa s]	E'_a [kJ mol^{-1}]	T_0 [K]	RMS	R^2
Protic Ionic Liquids					
$N_{2HHH}NO_3$[23]	0.283	-5.694	157.191	0.09078	1.0000
$N_{3HHH}NO_3$[23]	0.269	-6.328	162.927	0.18100	1.0000
$N_{4HHH}NO_3$[23]	0.116	-8.839	141.774	0.18900	0.9996
$N_{222H}TFA$[24]	0.042	-10.225	109.747	0.11580	0.9996
$N_{222H}MS$[24]	0.617	-4.147	203.83	0.44210	0.9997
$N_{222H}TfO$[24]	0.214	-7.273	139.503	0.04902	1.0000
Aprotic Ionic Liquids					
$Im_{11}TFSI$[9]	0.240	-5.238	174.073	0.13952	0.9984
$Im_{41}TFSI$[9]	0.254	-5.199	179.704	0.26445	0.9983
$Im_{41}BETI$[7]	0.125	-6.891	175.617	0.58351	0.9995
$Im_{41}TFA$[7]	0.096	-6.806	174.943	0.17590	0.9986
$Im_{41}TfO$[7]	0.129	-6.488	177.559	1.79432	0.9984
$Im_{81}TFSI$[8]	0.126	-7.005	170.213	0.26145	0.9990
$Pyr_{41}TFSI$[9]	0.229	-5.837	177.001	0.33525	0.9988
$Pyr_{31}FSI$ – $Pyr_{31}TFSI$ 3:2[25]	0.195	-7.189	137.966	0.1586	0.9999
Salt in Ionic Liquids					
$Pyr_{41}FSI$ – LiFSI 4:3[26]	0.207	-7.633	167.122	2.35200	0.9998
$Pyr_{31}FSI$ – Pyr_{31} TFSI – LiTFSI 12:7:1[25]	0.285	-6.301	153.264	0.2149	0.9998
$Pyr_{31}FSI$ – Pyr_{31} TFSI – LiTFSI 6:3:1[25]	0.273	-6.302	159.602	0.1619	0.9999
$Pyr_{31}FSI$ – Pyr_{31} TFSI – LiTFSI 3:1:1[25]	0.209	-7.454	153.162	0.3868	0.9999

Locally Concentrated Ionic Liquids					
$Pyr_{41}FSI$ – LiFSI – BTFE 4:3:4[26]	0.815	-4.337	178.244	0.82880	0.9992
$Pyr_{41}FSI$ – LiFSI – BTFE 2:1:2[27]	0.395	-5.258	170.147	0.20930	0.9999
$Im_{21}FSI$ – LiFSI – BTFE 2:1:2[27]	0.370	-4.485	179.721	0.88280	0.9975
$Im_{21}FSI$ – LiFSI – MFB 2:1:2[28]	0.678	-3.709	167.736	1.03100	0.9762
$Im_{21}FSI$ – LiFSI – DFB 2:1:2[29]	0.694	-3.417	179.259	0.52860	0.9956
Water-in-salt Electrolytes					
LiPTFSI : LiTfO 15m : 5m[30]	0.168	-7.269	158.418	0.40550	0.9999
LiPTFSI : LiTfO 19m : 5m[30]	0.150	-8.397	155.331	0.76330	1.0000
LiPTFSI 20m[30]	0.128	-7.923	157.74	0.38030	1.0000
Salt in Organic Solvent					
$LiPF_6$ 1M in EC:DMC 50:50[31]	0.173	-3.552	164.072	0.02171	0.9994

Table S8: VTF constrained fitting parameters obtained with IonFit for conductivity data.

System	σ_0 [mS cm^{-1}]	E'_a [kJ mol^{-1}]	T_0 [K]	RMS	R^2
Protic Ionic Liquids					
$N_{2HHH}NO_3$[23]	1482.070	4.909	157.191	0.05999	1.0000
$N_{3HHH}NO_3$[23]	1205.564	5.637	162.927	0.02076	1.0000
$N_{4HHH}NO_3$[23]	12.968	0.606	141.774	0.85145	0.1478
$N_{222H}TFA$[24]	839.059	9.864	109.747	0.008307	0.9999
$N_{222H}MS$[24]	183.258	3.627	203.83	0.01334	0.9999
$N_{222H}TfO$[24]	653.834	6.547	139.503	0.01507	1.0000
Aprotic Ionic Liquids					
$Im_{11}TFSI$[9]	555.004	4.274	174.073	0.03169	0.9999
$Im_{41}TFSI$[9]	448.471	4.691	179.704	0.06231	0.9997
$Im_{41}BETI$[7]	551.303	6.022	175.617	0.00780	0.9990
$Im_{41}TFA$[7]	828.281	5.731	174.943	0.00717	0.9999
$Im_{41}TfO$[7]	581.334	5.32	177.559	0.03496	0.9993
$Im_{81}TFSI$[8]	520.41	6.359	170.213	0.00410	0.9993
$Pyr_{41}TFSI$[9]	456.15	5.14	177.001	0.01231	0.9997
$Pyr_{31}FSI$ – $Pyr_{31}TFSI$ 3:2[25]	1517.907	7.081	137.966	0.4193	0.9988
Salt in Ionic Liquids					
$Pyr_{41}FSI$ – LiFSI 4:3[26]	683.915	6.872	167.122	0.03299	0.9983
$Pyr_{31}FSI$ – Pyr_{31} TFSI – LiTFSI 12:7:1[25]	987.738	6.16	153.264	0.211	0.9996
$Pyr_{31}FSI$ – Pyr_{31} TFSI – LiTFSI 6:3:1[25]	824.384	5.887	159.602	0.1141	0.9998
$Pyr_{31}FSI$ – Pyr_{31} TFSI – LiTFSI 3:1:1[25]	1738.062	7.413	153.162	0.0594	0.9999
Locally Concentrated Ionic Liquids					
$Pyr_{41}FSI$ – LiFSI – BTFE 4:3:4[26]	140.686	3.88	178.244	0.01656	0.9998
$Pyr_{41}FSI$ – LiFSI – BTFE 2:1:2[27]	189.541	3.94	170.147	0.02124	0.9999
$Im_{21}FSI$ – LiFSI – BTFE 2:1:2[27]	193.859	2.841	179.721	0.07732	0.9996
$Im_{21}FSI$ – LiFSI – MFB 2:1:2[28]	318.893	3.649	167.736	0.02686	0.9999
$Im_{21}FSI$ – LiFSI – DFB 2:1:2[29]	214.38	3.018	179.259	0.02017	1.0000
Water-in-salt Electrolytes					

LiPTFSI : LiTfO 15m : 5m[30]	680.439	5.361	158.418	0.02548	1.0000
LiPTFSI : LiTfO 19m : 5m[30]	697.66	6.247	155.331	0.01131	1.0000
LiPTFSI 20m[30]	777.847	5.599	157.74	0.03947	0.9999
Salt in Organic Solvent					
$LiPF_6$ 1M in EC:DMC 50:50[31]	152.388	2.863	164.072	0.07764	0.9997

Walden Analysis:

Walden plots represent the final step of the methodology proposed with IonFit. Albeit being lately criticized because of its over-simplistic assumptions[35], the Walden plot is still an extremely valid tool to be used as a rule of thumb in the quantification of the relationship between viscosity and conductivity. Moreover, it is possible to extract the Walden ionicity from the plot by calculating the vertical distance separating the experimental points from the ideal bisector line. Such a distance is denoted as ΔW and by applying the empirical rule

$$Walden\ ionicity = 10^{\Delta W} \quad \text{(S3)}$$

the Walden ionicity is readily obtained. Such a quantity is linked to the extent of ion pairing in the system, with completely dissociated electrolytes having a value of 1. The results of the Walden analysis performed with IonFit, are detailed in Table S9, and Figure S9.

Table S9: Walden fitting parameters obtained with IonFit.

System	α	C	RMS	R^2
Protic Ionic Liquids				
$N_{2HHH}NO_3$[23]	0.8697	0.8351	0.00232	0.9999
$N_{3HHH}NO_3$[23]	0.8969	0.6573	0.00188	0.9999
$N_{4HHH}NO_3$[23]	0.6749	0.6592	0.01131	0.9877
N_{222H}TFA[24]	1.005	0.0819	0.00666	0.9991
N_{222H}MS[24]	0.9151	0.1956	0.00980	0.9987
N_{222H}TfO[24]	0.9164	0.5117	0.00227	0.9999
Aprotic Ionic Liquids				
Im_{11}TFSI[9]	0.8313	0.9735	0.00391	0.9998
Im_{41}TFSI[9]	0.8867	0.5378	0.00153	1.0000
Im_{41}BETI[7]	0.8837	0.5635	0.00582	0.9998
Im_{41}TFA[7]	0.8524	0.4952	0.00290	0.9999
Im_{41}TfO[7]	0.8343	0.5742	0.01424	0.9985
Im_{81}TFSI[8]	0.9209	0.4394	0.00374	0.9999
Pyr_{41}TFSI[9]	0.892	0.6569	0.00487	0.9998
Pyr_{31}FSI – Pyr_{31}TFSI 3:2[25]	1.000	0.8161	0.00996	0.9980
Salt in Ionic Liquids				
Pyr_{41}FSI – LiFSI 4:3[26]	0.8869	0.4735	0.000741	1.0000
Pyr_{31}FSI – Pyr_{31} TFSI – LiTFSI 12:7:1[25]	0.9835	0.7922	0.009312	0.9984
Pyr_{31}FSI – Pyr_{31} TFSI – LiTFSI 6:3:1[25]	0.9419	0.7935	0.004529	0.9996
Pyr_{31}FSI – Pyr_{31} TFSI – LiTFSI 3:1:1[25]	0.9875	0.8742	0.02152	0.9939
Locally Concentrated Ionic Liquids				
Pyr_{41}FSI – LiFSI – BTFE 4:3:4[26]	0.8884	0.4835	0.009303	0.9983
Pyr_{41}FSI – LiFSI – BTFE 2:1:2[27]	0.7755	0.8222	0.001787	0.9999
Im_{21}FSI – LiFSI – BTFE 2:1:2[27]	0.6816	1.316	0.008033	0.9960
Im_{21}FSI – LiFSI – MFB 2:1:2[28]	1.000	0.5174	0.02046	0.9755
Im_{21}FSI – LiFSI – DFB 2:1:2[29]	0.9256	0.5725	0.008521	0.9957
Water-in-salt Electrolytes				
LiPTFSI : LiTfO 15m : 5m[30]	0.7555	1.215	0.002378	0.9999
LiPTFSI : LiTfO 19m : 5m[30]	0.7590	1.088	0.000381	1.0000

LiPTFSI 20m[30]	0.7253	1.567	0.001456	1.0000
Salt in Organic Solvent				
$LiPF_6$ 1M in EC:DMC 50:50[31]	0.8607	0.1028	0.000414	1.0000

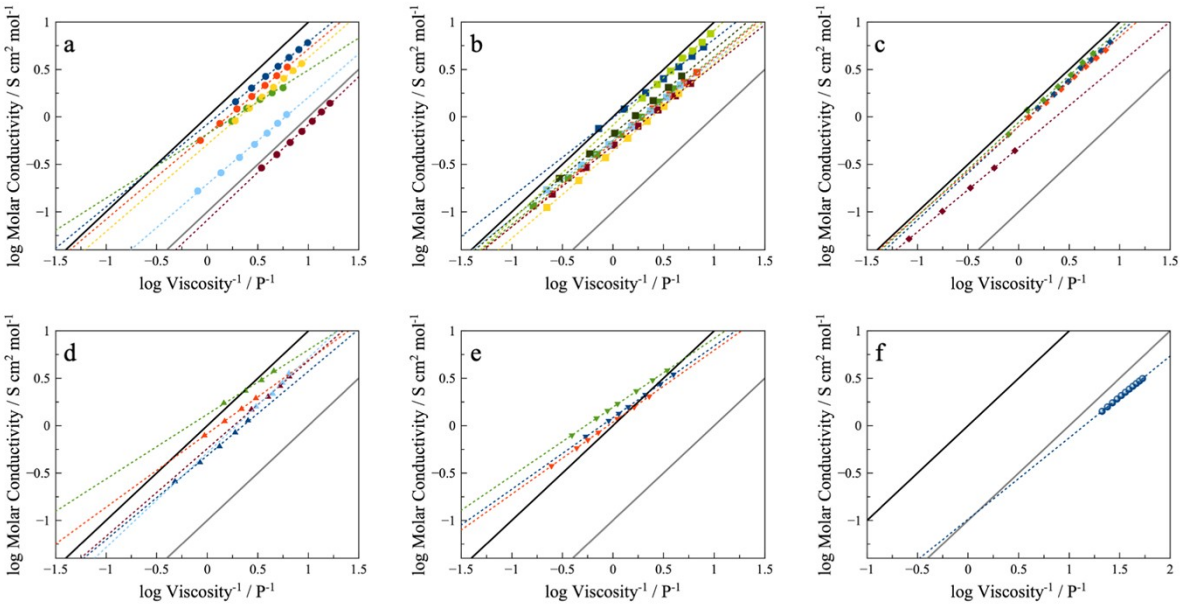

Figure S9: Results of the Walden analysis on the systems in Table S6. The continuous black line is the "ideal" limit, while the continuous gray line is the reference for poor ionicity. (a) Protic Ionic Liquids, (b) Aprotic Ionic Liquids, (c) Salt in Ionic Liquid, (d) Locally Concentrated Ionic Liquid Electrolytes, (e) Water-in-Salt Electrolytes, (f) Salt in Organic Solvent. For each panel, the color order is blue, red, green, brown, cyan, yellow, gray, light green. The order corresponds to the order in Table S6.

Abbreviations

N_{2HHH}	Ethylammonium
N_{3HHH}	Propylammonium
N_{4HHH}	Butylammonium
N_{222H}	Triethylammonium
Im_{11}	N,N'-dimethylimidazolium
Im_{21}	N-ethyl-N'-methylimidazolium
Im_{41}	N-butyl-N'-methylimidazolium
Im_{81}	N-methyl-N'-octylimidazolium
Pyr_{31}	N-methyl-N-propylpyrrolidinium
Pyr_{41}	N-butyl-N-methylpyrrolidinium
NO3	Nitrate
TFA	Trifluoroacetate
MS	Mesylate
TfO	Triflate
FSI	bis(fluorosulfolyl)imide
TFSI	bis(trifluoromethylsulfonyl)imide
BETI	Bis (pentafluoroethylsulfonyl)imide

PTFSI	Bis (pentafluoroethylsulfonyl)imide
BTFE	Bis(2,2,2-trifluoroethyl) ether
MFB	Monofluorobenzene
DFB	1,2-difluorobenzene
EC	Ethylencarbonate
DMC	Dimethylcarbonate

References

[1] H. J. Backer, *Recl. Trav. Chim. Pays-Bas* 1929, *48*, 949.
[2] H. Goldwhite, M. S. Gibson, C. Harris, *Tetrahedron* 1965, *21*, 2743.
[3] A. Bocarsly, E. Niangar, *Encyclopedia of Electrochemical Power Sources*, Elsevier, 2009.
[4] H. Hou, H. M. Schütz, J. Giffin, K. Wippermann, X. Gao, A. Mariani, S. Passerini, C. Korte, *ACS Appl. Mater. Interfaces* 2021, *13*, 8370.
[5] M. Martinez, Y. Molmeret, L. Cointeaux, C. Iojoiu, J. C. Leprêtre, N. El Kissi, P. Judeinstein, J. Y. Sanchez, *J. Power Sources* 2010, *195*, 5829.
[6] H. Hou, H. M. Schütz, J. Giffin, K. Wippermann, X. Gao, A. Mariani, S. Passerini, C. Korte, *ACS Appl. Mater. Interfaces* 2021, *13*, 26649.
[7] H. Tokuda, K. Hayamizu, K. Ishii, M. A. B. H. Susan, M. Watanabe, *J. Phys. Chem. B* 2004, *108*, 16593.
[8] H. Tokuda, K. Hayamizu, K. Ishii, M. A. B. H. Susan, M. Watanabe, *J. Phys. Chem. B* 2005, *109*, 6103.
[9] H. Tokuda, K. Ishii, Md. A. B. H. Susan, S. Tsuzuki, K. Hayamizu, M. Watanabe, *J. Phys. Chem. B* 2006, *110*, 2833.
[10] J. O. Bockris, A. K. N. Reddy, *Modern Electrochemistry 1*, Plenum Press, New York, 1998.
[11] A. Mariani, R. Caminiti, F. Ramondo, G. Salvitti, F. Mocci, L. Gontrani, *J. Phys. Chem. Lett.* 2017, *8*, 3512.
[12] K. Fumino, A. Wulf, R. Ludwig, *Angew. Chem. Int. Ed.* 2009, *48*, 3184.
[13] F. Neese, F. Wennmohs, U. Becker, C. Riplinger, *J. Chem. Phys.* 2020, *152*, 224108.
[14] J. W. Furness, A. D. Kaplan, J. Ning, J. P. Perdew, J. Sun, *J. Phys. Chem. Lett.* 2020, *11*, 8208.
[15] P. Pracht, F. Bohle, S. Grimme, *Phys. Chem. Chem. Phys.* 2020, *22*, 7169.
[16] C. Bannwarth, S. Ehlert, S. Grimme, *J. Chem. Theory Comput.* 2019, *15*, 1652.
[17] V. Barone, M. Cossi, *J. Phys. Chem. A* 1998, *102*, 1995.
[18] A. V. Marenich, C. J. Cramer, D. G. Truhlar, *J. Phys. Chem. B* 2009, *113*, 6378.
[19] V. Ásgeirsson, B. O. Birgisson, R. Bjornsson, U. Becker, F. Neese, C. Riplinger, H. Jónsson, *J. Chem. Theory Comput.* 2021, *17*, 4929.
[20] Y.-S. Lin, G.-D. Li, S.-P. Mao, J.-D. Chai, *J. Chem. Theory Comput.* 2013, *9*, 263.
[21] C. Bannwarth, E. Caldeweyher, S. Ehlert, A. Hansen, P. Pracht, J. Seibert, S. Spicher, S. Grimme, *WIREs Comput. Mol. Sci.* 2021, *11*, e1493.
[22] D. Turnbull, M. H. Cohen, *J. Chem. Phys.* 1961, *34*, 120.
[23] J. N. Canongia Lopes, J. M. S. S. Esperança, A. M. de Ferro, A. B. Pereiro, N. V. Plechkova, L. P. N. Rebelo, K. R. Seddon, I. Vázquez-Fernández, *J. Phys. Chem. B* 2016, *120*, 2397.
[24] A. Mariani, M. Bonomo, X. Gao, B. Centrella, A. Nucara, R. Buscaino, A. Barge, N. Barbero, L. Gontrani, S. Passerini, *J. Mol. Liq.* 2021, *324*, 115069.
[25] M. Moreno, E. Simonetti, G. B. Appetecchi, M. Carewska, M. Montanino, G.-T. Kim, N. Loeffler, S. Passerini, *J. Electrochem. Soc.* 2017, *164*, A6026.
[26] X. Liu, M. Zarrabeitia, A. Mariani, X. Gao, H. M. Schütz, S. Fang, T. Bizien, G. A. Elia, S. Passerini, *Small Methods* 2021, *5*, DOI 10.1002/smtd.202100168.
[27] X. Liu, A. Mariani, M. Zarrabeitia, M. E. Di Pietro, X. Dong, G. A. Elia, A. Mele, S. Passerini, *Energy Storage Mater.* 2022, *44*, 370.
[28] X. Liu, T. Diemant, A. Mariani, X. Dong, M. E. Di Pietro, A. Mele, S. Passerini, *Adv. Mater.* 2022, *34*, 2207155.

[29] X. Liu, A. Mariani, T. Diemant, M. E. D. Pietro, X. Dong, M. Kuenzel, A. Mele, S. Passerini, *Adv. Energy Mater.* 2022, *12*, 2200862.
[30] G. Horwitz, C. R. Rodríguez, P. Y. Steinberg, G. Burton, H. R. Corti, *Electrochimica Acta* 2020, *359*, 136915.
[31] P. Porion, Y. R. Dougassa, C. Tessier, L. El Ouatani, J. Jacquemin, M. Anouti, *Electrochimica Acta* 2013, *114*, 95.
[32] D. H. Vogel, *Phys. Z.* 1921, *22*, 645.
[33] G. Tammann, W. Hesse, *Z. Für Anorg. Allg. Chem.* 1926, *156*, 245.
[34] G. S. Fulcher, *J. Am. Ceram. Soc.* 1925, *8*, 339.
[35] C. Schreiner, S. Zugmann, R. Hartl, H. J. Gores, *J. Chem. Eng. Data* 2010, *55*, 1784.